

VLBA determination of the distance to nearby star-forming regions

VII. Monoceros R2

Sergio A. Dzib¹, Gisela N. Ortiz-León², Laurent Loinard^{1,2}, Amy J. Mioduszewski³, Luis F. Rodríguez^{2,4}, Rosa M. Torres⁵, and Adam Deller⁶

ABSTRACT

We present a series of sixteen Very Long Baseline Array (VLBA) high angular resolution observations of a cluster of suspected low-mass young stars in the Monoceros R2 region. Four compact and highly variable radio sources are detected; three of them in only one epoch, the fourth one a total of seven times. This latter source is seen in the direction to the previously known UCH II region VLA 1, and has radio properties that resemble those of magnetically active stars; we shall call it VLA 1*. We model its displacement on the celestial sphere as a combination of proper motion and trigonometric parallax. The fit obtained using a uniform proper motion yields a parallax $\varpi = 1.10 \pm 0.18$ mas, but with a fairly high post-fit dispersion. If acceleration terms (probably due to an undetected companion) are included, the quality of the fit improves dramatically, and the best estimate of the parallax becomes $\varpi = 1.12 \pm 0.05$ mas. The magnitude of the fitted acceleration suggest an orbital period of order a decade. The measured parallax corresponds to a distance $d = 893^{+44}_{-40}$ pc, in very good agreement with previous, indirect, determinations.

Subject headings: astrometry — radio continuum: stars — radiation mechanisms: non-thermal — techniques: interferometric

1. Introduction

Very Long Baseline Interferometry (VLBI) at radio frequencies is an observing technique that provides images with very high angular resolu-

tion (of order 1 mas at $\nu \sim 10$ GHz) and very accurate astrometric registration relative to distant quasars (typically better than 0.1 mas, even in moderate signal-to-noise situations; e.g. Reid & Honma 2014). An interesting application of these characteristics is the direct determination of distances through the accurate measurement of trigonometric parallaxes using multi-epoch VLBI observations. Magnetically active Young Stellar Objects (YSOs) have been a target of choice because they are associated with bright and compact radio sources that can easily be detected in VLBI observations (e.g. Loinard et al. 2005, 2007, 2008; Menten et al. 2007; Torres et al. 2007, 2009, 2012; Dzib et al. 2010, 2011; Ortiz-León et al. 2016, in preparation). VLBI observations are particularly appropriate for the case of young stars (e.g., Loinard et al. 2011; Brunthaler et al. 2011) because they are often highly embedded inside of their parental cloud, and therefore highly ob-

¹Max Planck Institut für Radioastronomie, Auf dem Hügel 69, 53121 Bonn, Germany (sdzib@mpifr-bonn.mpg.de)

²Instituto de Radioastronomía y Astrofísica, Universidad Nacional Autónoma de México Apartado Postal 3-72, 58090, Morelia, Michoacán, Mexico

³National Radio Astronomy Observatory, Domenici Science Operations Center, 1003 Lopezville Road, Socorro, NM 87801, USA

⁴El Colegio Nacional, Donceles 104, 06020, México, DF, México

⁵Instituto de Astronomía y Meteorología, Universidad de Guadalajara, Avenida Vallarta No. 2602, Col. Arcos Vallarta, CP 44130, Guadalajara, Jalisco, México

⁶ASTRON, The Netherlands Institute for Radio Astronomy, Postbus 2, 7990 AA, Dwingeloo, The Netherlands

scured. As a consequence, optical and near-IR telescopes (including the Gaia astrometry mission) are at a disadvantage for this type of sources. In this paper, we will present multi-epoch VLBI observations of a suspected cluster of magnetically active low-mass YSOs in the Monoceros R2 high-mass star-forming region.

The Monoceros R2 region was initially identified as a chain of reflection nebulae illuminated by A- and B-type stars (Gyulbudaghian et al. 1978 and references therein) and named GGD 11 to 17. Those nebulae are associated with a giant molecular cloud that harbors numerous other signposts of active massive star-formation (water masers, bright infrared sources, etc.). Indeed, one of the first molecular outflows ever reported (Rodríguez et al. 1982) is located in the GGD 12–15 sub-region of Monoceros. In this very same region, Gómez et al. (2000, 2002) discovered a cluster of nine compact radio sources surrounding a cometary Ultra Compact H II region (UCH II), and distributed over an area of less than 400 arcsec^2 . The UCH II region was named VLA 1 and the compact sources VLA 2 to VLA 10. Gómez et al. (2000, 2002) argued that most of these compact radio sources are associated with magnetically active low-mass YSOs because of their variability and spectral indices. As a consequence, they are good candidates for VLBI observations.

Obtaining an accurate distance to Monoceros is of high importance since it is, after Orion at $414 \pm 7 \text{ pc}$ (Menten et al. 2007) and Cepheus A at $700 \pm 30 \text{ pc}$ (Moscadelli et al. 2009; Dzib et al. 2011), one of the nearest regions where high-mass star formation is occurring. Distances to Monoceros R2 have been estimated mainly using spectroscopic and photometric studies. The first measurements are from Racine (1968), who estimated a distance of $830 \pm 50 \text{ pc}$; and Rozhkovski & Kurchakov (1968) who found a distance of 700 pc (see also Downes et al. 1975). Later on, Racine & Van der Bergh (1970), in a proceeding conference, gave a revised distance of 950 pc , without further details. In the most recent paper using that technique, Herbst & Racine (1976) reported $830 \pm 50 \text{ pc}$; this last value is the most commonly adopted distance to Monoceros R2 in the astronomical literature (Carpenter & Hodapp 2008). On the other hand, Rodríguez et al. (1980) use CO line observations to derive a kinematic distance of 1 kpc , which

is another commonly used distance for Monoceros R2. Finally, Reid et al. (2016) have made available a bayesian distance calculator that improves the determination of the kinematic distances to sources in the galactic spiral arms. By using this tool and a $v_{lsr} = +11 \pm 1 \text{ km s}^{-1}$ for GGD 12–15 (Rodríguez et al. 1980) we obtained two possible distances. The most likely distance, with a probability density of 17 kpc^{-1} , is $760 \pm 70 \text{ pc}$ that is in agreement with the distance obtained by Herbst & Racine (1976). The second possible distance, with a probability density of just 5 kpc^{-1} , is around 420 pc .

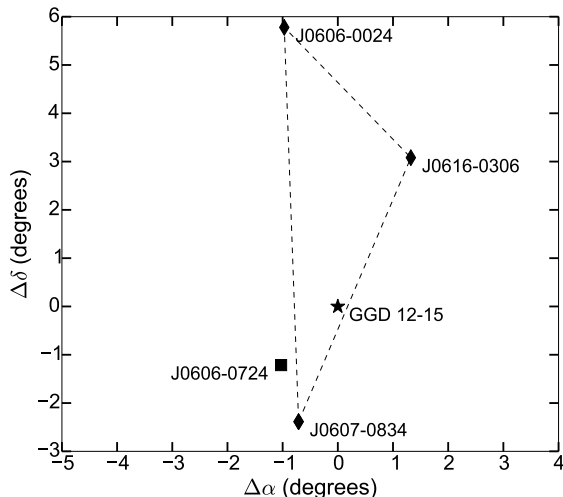


Fig. 1.— Positions of the main (black square) and secondary calibrators (black diamonds) relative to the target position (black star).

2. Observations

We observed the 10 VLA sources from Gómez et al. (2000, 2002) using the VLBI technique. Specifically, the observations were collected using the Very Long Baseline Array (VLBA; Napier et al. 1994) operated in combination with the 100-m Robert C. Byrd Green Bank telescope (GBT; Prestage et al. 2009) at a wavelength of 3.6 cm ($\nu = 8.42 \text{ GHz}$). A total of 17 observations were performed (see Table 1). We first undertook a pilot study (BL169) which consisted of three epochs, in which we detected three sources. Following the successful detection of three of the target

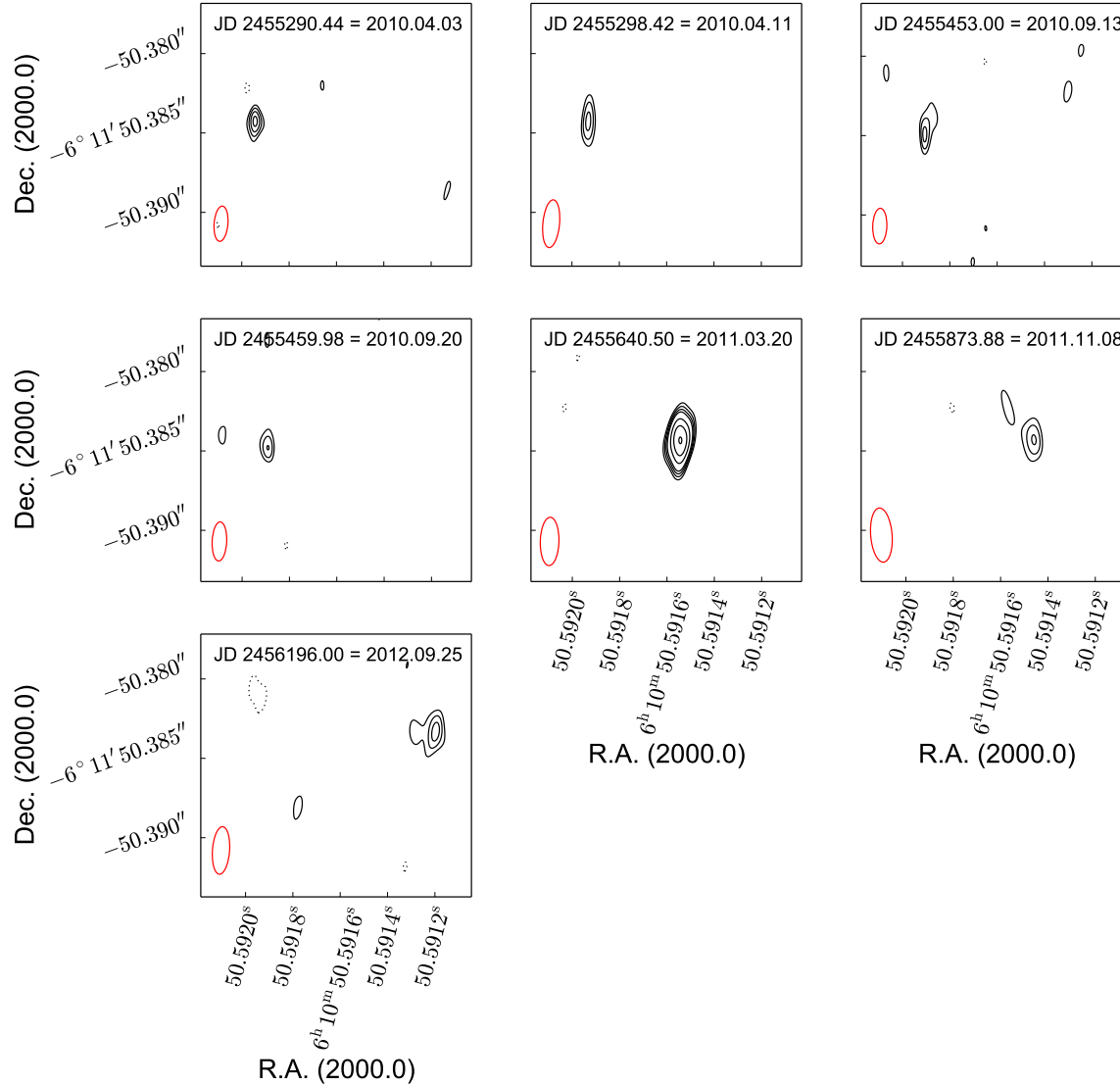


Fig. 2.— Images of VLA 1* at the six detected epochs. The synthesized beam is displayed as a red ellipse at the bottom left of each panel. The contour levels are -3, 3, 4, 5, 6, 9, 12, and 15 times the noise level in each image, which are given in Table 1.

sources, we initiated a series of multi-epoch observations starting in September 2010, as part of the project BL176. The observations, including the pilot epochs, were accommodated close to the equinoxes when the maximum elongation of the parallactic ellipse occurs (specifically for Monoceros, the maximum elongation occurs on March and September 24 of each year). During each equinox a maximum of three observations were

scheduled separated from one another by a few days to a few weeks. As the sources are highly variable, this observing mode increases the probability of obtaining at least one detection during each equinox. The last observation was collected in October 2012.

The spectral setups were different for projects BL169 and BL176. In the former, four base-band

channels (BBCs) were observed. Each BBCs contained 128 channels of 0.125 MHz each. This setup was chosen to enable the mapping of the entire area containing our 10 targets without significant bandwidth smearing loss. The BL176 observations, on the other hand, used only 16 channels of 1 MHz each, but took advantage of the (then, newly available) multi-phase center capability provided by the VLBA DifX digital correlator (Deller et al. 2011). In this observing mode, a different phase center was positioned at the location of each one of our 10 targets, generating 10 separate and smaller visibility datasets.

The main phase calibrator for all epochs was J0606–0724, located at an angular distance of 1.6 degrees from the targets. To improve the quality of phase calibration, we also observed the secondary calibrators J0607–0834, J0616–0306 and J0606–0024, which are distributed around our target sources as shown in Figure 1. Additionally, about two dozen ICRF quasars spread over the entire visible sky were observed periodically during the observations (conforming so-called *geodetic blocks*); those are used to improve tropospheric calibration (e.g., Reid & Brunthaler 2004). The observations obtained as part of project BL169 had a total duration of five hours while those corresponding to project BL176 had a duration of nine hours. Each individual observation contained three 30-minute geodetic blocks, scheduled at the beginning, the middle, and the end of each observation. The observations of the targets were recorded as part of cycles with two minutes spent on-source, and one minute spent on the main phase calibrator. Roughly every 30 minutes, we also observed the secondary calibrators, spending one minute on each one.

Two of the observations were affected by logistical issues and were excluded from our analysis: Epoch BL176l was a total loss, with no usable data recorded, while epoch BL176h was affected by a mistake during correlation which led to no dataset being produced for the target phase centers. Additionally, in the epoch BL176f the setup used to observe the ICRF quasars was erroneously kept until half-way through the observations, meaning the first half of the target data was unusable. This limited the observing time, and explains the higher noise level recorder in that observation (Table 1). In epoch BL176m the Tsys information for the

GBT antenna was not generated, and it was artificially created a posteriori using the Tsys information from the epoch BL176c that was taken almost on the same date but two years before. In this case we down-weighted the visibilities containing GBT data to minimize the impact of the resulting poorer amplitude calibration. We note that the calibrator data are self-calibrated in amplitude as part of the data processing. This helped to mitigate the lack of Tsys measurements for the GBT. Finally for epochs BL176d and BL176e the field related to source VLA 9 was not correlated.

The data were edited and calibrated using the Astronomical Image Processing System (AIPS; Greisen 2003). The basic data reduction followed the standard VLBA procedure for phase-referenced observations, including the multi-calibrator schemes and the tropospheric and clock corrections obtained from the geodetic blocks. These calibrations were described in detail by Loinard et al. (2007), Torres et al. (2007) and Dzib et al. (2010). After calibration, the visibilities were first imaged with a pixel size of $50 \mu\text{as}$ using a natural weighting scheme¹ (ROBUST = 5 in AIPS). As this scheme provides the best possible noise levels, we used these images to search for source detections. When a detection was obtained, we constructed new images with a weighting scheme intermediate between natural and uniform (ROBUST = 0 or ROBUST = 2, depending on the intensity of the detection). This enabled a slightly better determination of the source positions at each epoch. The r.m.s. noise levels in the final images were $18 - 41 \mu\text{Jy beam}^{-1}$. The pa-

¹ The weighting schemes are derived and discussed by Briggs (1995). Briefly, the ROBUST parameter specifies how the visibilities are weighted before imaging. With ROBUST = +5 (natural weighting), the visibilities are weighted according to their density in the (u, v) plane. This leads to the best possible noise level, but since the central portion of the (u, v) plane tends to be more densely populated than the outer parts, natural weighting produces the lowest possible angular resolution. ROBUST = -5 (uniform weighting), on the other, produces a uniform weighting of the visibilities across the (u, v) plane. This results in the highest possible resolution, but worst possible noise level. Intermediate values (in AIPS, ROBUST varies continuously between the ± 5 extrema) correspond to intermediate weighting schemes between natural and uniform. In many cases, ROBUST values around zero provide a good compromise yielding a substantial gain in resolution over natural weighting, at the cost of only a minor loss in sensitivity.

rameters of images in individual epochs are given in Table 1. From these images, the source position, when detected, was determined by using a two-dimensional fitting procedure (task JMFIT in AIPS). The brightness temperature was calculated following:

$$T_b[\text{K}] \simeq 6.26 \times 10^6 \left(\frac{S_\nu}{\text{mJy}} \right) \left(\frac{\theta_{\text{maj}}}{\text{mas}} \right)^{-1} \left(\frac{\theta_{\text{min}}}{\text{mas}} \right)^{-1},$$

where θ_{maj} and θ_{min} are the semi-major and semi-minor axis of the deconvolved source size determined by JMFIT.

Table 1: Observation summary.

Project ^a	UT date (yyyy.mm.dd)	Synthesized beam ($\theta_{\text{maj}} \times \theta_{\text{min}}$; P.A.)	σ_{noise} ($\mu\text{Jy bm}^{-1}$)
BL169a	2010.03.28	0''0034 \times 0''0010; -6.0°	25
BL169b	2010.04.03	0''0033 \times 0''0010; -6.4°	23
(R0)		0''0022 \times 0''0009; -4.7°	35
BL169c	2010.04.11	0''0036 \times 0''0011; -6.3°	24
(R2)		0''0030 \times 0''0011; -5.4°	27
BL176a	2010.09.13	0''0033 \times 0''0011; -5.1°	18
(R0)		0''0022 \times 0''0009; -2.0°	25
BL176b	2010.09.20	0''0033 \times 0''0011; -5.2°	19
(R0)		0''0025 \times 0''0009; -2.5°	26
BL176c	2010.09.26	0''0033 \times 0''0011; -4.3°	20
BL176d	2011.03.20	0''0035 \times 0''0012; -3.0°	18
(R0)		0''0023 \times 0''0010; +0.2°	26
BL176e	2011.03.25	0''0037 \times 0''0011; -4.4°	20
BL176f	2011.09.15	0''0025 \times 0''0011; +3.9°	41
BL176g	2011.09.19	0''0057 \times 0''0017; -12.0°	24
BL176h	2011.09.26
BL176i	2011.11.06	0''0037 \times 0''0012; -3.8°	18
BL176j	2011.11.08	0''0036 \times 0''0013; 0.5°	20
BL176k	2012.04.01	0''0033 \times 0''0012; -4.2°	18
BL176l	2012.09.20
BL176m	2012.09.25	0''0030 \times 0''0011; -4.1°	18
BL176n	2012.10.01	0''0036 \times 0''0011; -3.9°	17

^aThe first line for each observation shows the parameters of the images obtained with natural weighting (ROBUST = 5). When a second line is present, it contains information on images reconstructed for the same epoch, but with a different weighting scheme: R0 and R2 stand for ROBUST = 0 and ROBUST = 2, respectively (see text).

3. Results

A total of four distinct sources were detected in our observations. A source associated with VLA 1 was detected seven times (Figure 2). Additionally, we detected a source associated with VLA 3 at 10σ , a source associated with VLA 8 at 11σ , and a source associated with VLA 10 at 6σ . All three of these cases, however, were single-epoch detections. The parameters of all detections are

given in Table 2. In most cases, the deconvolved size for the detected sources was consistent with a point-like structure. In two cases the source could be modeled with a slightly resolved source, although a point-like structure cannot be discarded. Given the measured flux densities and the compactness of the emission, each of the detections implies brightness temperatures in excess of $\sim 10^6$ K (Table 2). In addition, the sources appear to be highly variable: the VLBA source associated with VLA 1 shows variations by a factor of nearly 5, while the sources associated with VLA 3, 8, and 10 should have been detected at most epochs if their fluxes remained steady. The fact that they were not suggests that they go through occasional flaring activity when their flux increases at least by a factor of several. This combination of high brightness temperature and high variability strongly suggests that the detected sources are flaring low-mass stars with coronal emission. This was previously suggested for VLA 3, VLA 8 and VLA 10 by Gómez et al. (2000, 2002), but it was not expected for VLA 1 since this latter source traces an UCH II region. We will call VLA 1* the VLBA source detected here toward VLA 1, and discuss its nature further in the upcoming section.

4. Discussion

4.1. The distance to Monoceros

The positions of VLA 1* measured in our seven VLBA detections can be modeled as a combination of a trigonometric parallax (ϖ) and proper motion (μ) following e.g. Loinard et al. (2007). The barycentric coordinates of the Earth appropriate for each observation were calculated using the NOVAS routines distributed by the US Naval Observatory. The reference epoch was taken at JD 2455743.22 \equiv J2011.49, the mean epoch of our detections. The best fit to the data assuming a uniform proper motion (Figure 4, top) yields the following astrometric elements:

$$\begin{aligned} \alpha_{J2011.49} &= 06^{\text{h}}10^{\text{m}}50^{\text{s}}591549 \pm 0^{\text{s}}000012 \\ \delta_{J2011.49} &= -06^{\circ}11'50''38412 \pm 0''00010 \\ \mu_{\alpha} \cos \delta &= -5.35 \pm 0.21 \text{ mas yr}^{-1} \\ \mu_{\delta} &= 0.45 \pm 0.12 \text{ mas yr}^{-1} \\ \varpi &= 1.10 \pm 0.18 \text{ mas.} \end{aligned}$$

Table 2: Calendar and Julian dates, measured source positions, flux densities, noise levels, and brightness temperatures of detections.

Mean UT date (yyyy.mm.dd/hh:mm)	Julian Day	α (J2000.0) 06 ^h 10 ^m	σ_α	δ (J2000.0) −06 ^o	σ_δ	f_ν (mJy)	T_b (10 ⁶ K)
VLA 1							
2010.04.03/22:33	2455290.44	50 ^s 591943	0 ^s 0000048	11′ 50″38440	0″00013	0.23±0.04 ^a	>3.0 ^c
2010.04.11/22:04	2455298.42	50 ^s 591930	0 ^s 0000045	11′ 50″38429	0″00027	0.15±0.03 ^b	>1.9 ^c
2010.09.13/12:00	2455453.00	50 ^s 591896	0 ^s 0000053	11′ 50″38454	0″00026	0.17±0.05 ^a	>2.2 ^c
2010.09.20/11:31	2455459.98	50 ^s 591893	0 ^s 0000058	11′ 50″38463	0″00020	0.23±0.03 ^a	>2.5 ^c
2011.03.20/00:00	2455640.50	50 ^s 591548	0 ^s 0000023	11′ 50″38434	0″00008	0.45±0.03 ^a	>2.0 ^d
2011.11.08/09:07	2455873.88	50 ^s 591464	0 ^s 0000081	11′ 50″38442	0″00026	0.10±0.03	>0.5 ^c
2012.09.25/12:03	2456196.00	50 ^s 591200	0 ^s 0000072	11′ 50″38337	0″00024	0.10±0.02	>0.2 ^c
VLA 3							
2010.03.28/23:00	2455284.46	49 ^s 945410	0 ^s 0000029	11′ 45″82133	0″00012	0.26±0.03	>1.9 ^c
VLA 8							
2011.03.26/01:15	2455646.55	49 ^s 212366	0 ^s 0000033	11′ 29″93380	0″00015	0.28±0.04	>0.5 ^d
VLA 10							
2010.04.11/22:04	2455298.42	50 ^s 504350	0 ^s 0000051	12′ 04″21946	0″00023	0.15±0.03	>1.2 ^c

^aFrom image produced with ROBUST=0.

^bFrom image produced with ROBUST=2.

^cSource is unresolved, we used the size of the synthesized beam as the nominal size.

^dSource can be resolved but can also be a point source, we used the maximum fitted size to place a lower limit on the brightness temperature.

The post-fit r.m.s. values, however, are fairly large: 0.27 and 0.16 mas in right ascension and declination, respectively. Indeed, systematic errors of 0.40 mas and 0.13 mas (in right ascension and declination, respectively) had to be added in quadrature to the uncertainties delivered by JMFIT to obtain a reduced χ^2 of 1.

The situation can be very significantly improved if the proper motion is allowed to be (uniformly) accelerated. The best fit, in this case (Figure 4, bottom) yields:

$$\begin{aligned}
\alpha_{J2011.49} &= 06^h10^m50^s591523 \pm 0^s000005 \\
\delta_{J2011.49} &= -06^\circ11'50''38422 \pm 0''00009 \\
\mu_\alpha \cos \delta &= -5.32 \pm 0.07 \text{ mas yr}^{-1} \\
\mu_\delta &= 0.50 \pm 0.10 \text{ mas yr}^{-1} \\
a_\alpha \cos \delta &= 0.92 \pm 0.11 \text{ mas yr}^{-2} \\
a_\delta &= 0.37 \pm 0.14 \text{ mas yr}^{-2} \\
\varpi &= 1.12 \pm 0.05 \text{ mas.}
\end{aligned}$$

From the comparison with the non-accelerated case, it can be seen that the situation in declination remains nearly unchanged, with an acceleration component in that direction consistent with 0 within 2.5σ . In right ascension, however, the fit is significantly improved, with an acceleration com-

ponent detected at nearly 9σ and an improvement on the final parallax accuracy by a factor of 3. This improvement also results in the fact that to obtain a reduced χ^2 of 1, no systematic errors at all had to be added to those delivered by JMFIT in declination. In right ascension, only 0.09 mas had to be added (compared with 0.33 mas when no acceleration is allowed). Note that the best-fit value of the parallax remains, nevertheless, fully consistent with the non-accelerated case.

The existence of acceleration in the proper motion of VLA 1* suggests that it belongs to a multiple system. The acceleration vector does not appear to point toward any of the known sources associated with VLA 1. In addition, the amplitude of the acceleration appears to be fairly substantial (nearly 1 mas yr^{−2}, compared with a proper motion of about 5 mas yr^{−1} along that same direction) so the companion must be very nearby. We are most likely dealing with a very compact binary stellar system.

Since the acceleration can be approximated with a constant value over the interval of 2.5 years spanned by the observations, we can conservatively conclude that the period of the binary must be significantly longer than 2.5 years (e.g., see Figure 5). If we assume that the binary system

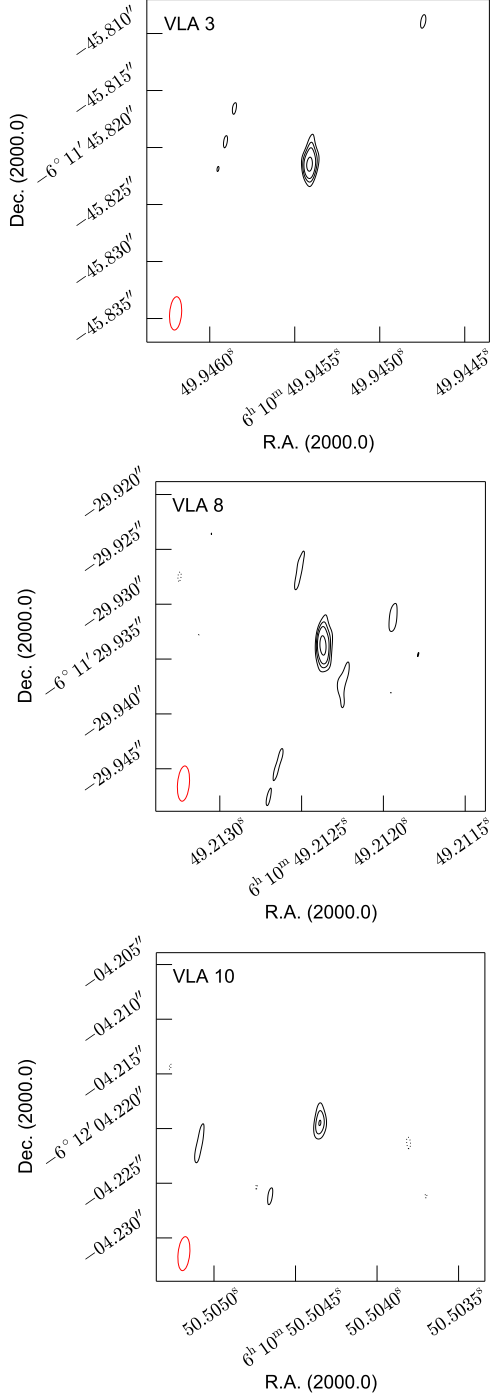


Fig. 3.— Similar as Figure 2 but for the detection of VLA 3, VLA 8 and VLA 10. The contour levels are -3, 3, 4.5, 6 and 9 times the noise level.

is formed by two stars each with one solar mass and that the orbit is circular and face-on, we will get the largest acceleration possible in the plane of the sky. This gives an upper limit to the separation for the components of the binary of 6.5 AU. In turn, this gives an upper limit to the period of 12.2 years. We conclude that our results are consistent with a binary system with these parameters. Since acceleration is not constant along a Keplerian orbit, future observations ought to be inconsistent with our constant acceleration assumption. In particular, observations obtained in the next few years should, if fitted independently of the data presented here, yield a different acceleration vector.

The best fit to our data implies a parallax $\varpi = 1.12 \pm 0.05$ mas, corresponding to a distance $d = 893^{+42}_{-40}$ pc. This result is, within errors, in agreement with the distance of 830 ± 50 pc obtained by Herbst & Racine (1976), and the kinematic distance of Rodríguez et al. (1980). It should be emphasized, however, that the previous measurements were indirect and, therefore, prone to possible systematic errors related with uncertain assumptions regarding the nature of the observed star, the properties of the interstellar medium, or the appropriate Galactic rotation curve. Our measurement, on the other hand, is purely geometric.

4.2. Galactic kinematics of Monoceros

It has been suggested that Monoceros and Orion might be linked by an expanding superbubble that may have triggered star-formation in both regions (Heiles 1998). From the distance to Monoceros reported above and its measured proper motion and radial velocity ($v_{lsr} = +11 \pm 1$ km s⁻¹; see Rodríguez et al. 1980), one can derive the location (x, y, z) and velocity vector (u, v, w) of Monoceros in the Milky Way, and examine this issue from a kinematic point of view. We will express the positions and velocities in the commonly used rectangular reference frame centered on the location of the Sun, with the (Ox) axis pointing toward the Galactic center, the (Oy) axis perpendicular to (Ox) and pointing in the direction of Galactic rotation, and (Oz) pointing toward the Galactic North Pole (GNP) so as to make $(Oxyz)$ right-handed. In these coordinates, the position of Monoceros appears to be $(x, y, z) = (-846, -6, -283)$ pc: it is located almost ex-

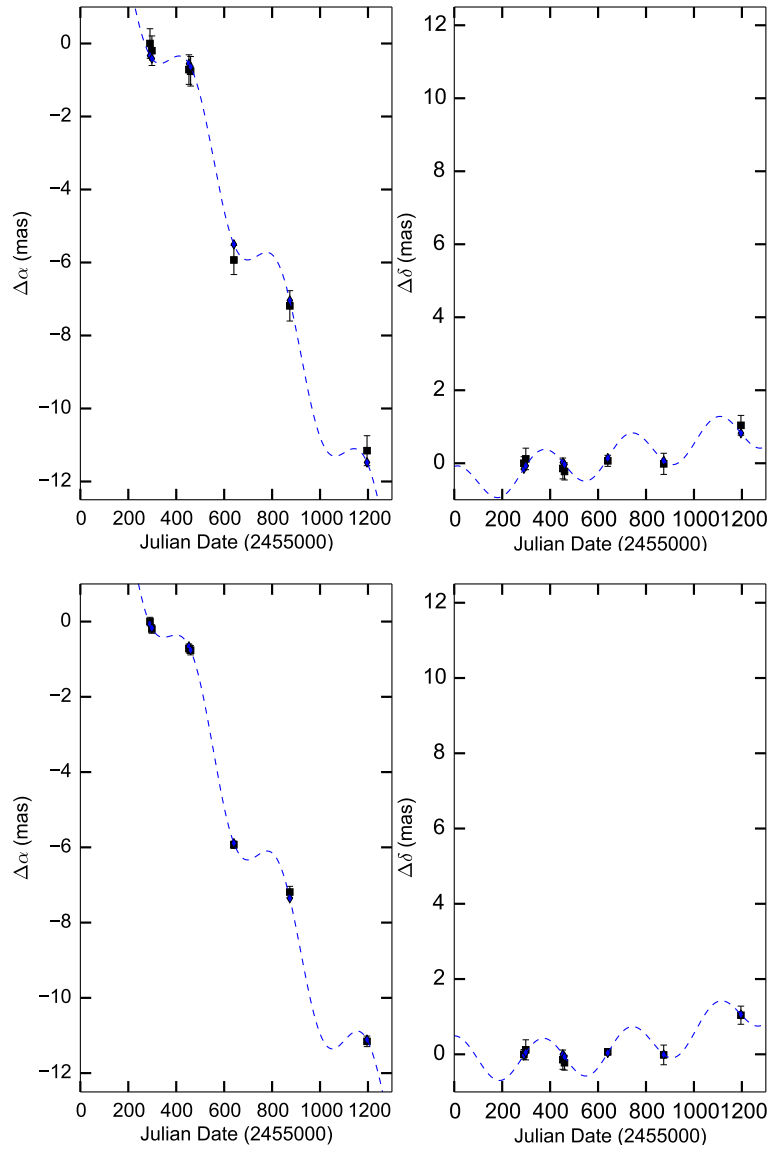


Fig. 4.— The observed VLA 1* positions for right ascension (left panels) and declination (right panels) are plotted as black filled squares. The dotted curves show the best fit to the trajectory of the star as a combination of the trigonometric parallax and uniform proper motion (top panels) and also including uniform acceleration (bottom panels). Blue filled squares are the expected position according to the fit.

actly toward the Galactic anticenter, but nearly 300 pc below the Galactic mid-plane. For reference, in the same system, Orion is located at $(-393, -3, -131)$ pc, nearly the same direction but at less than half the distance.

The velocity vector of Monoceros deduced from

our observations, and expressed in the same rectangular frame relative to the LSR is $(u, v, w) = (-25.4, -10.3, -14.7)$ km s^{-1} with formal uncertainties of order 2 km s^{-1} along each direction. We note, however, that since this value is based on a single proper motion measurement, it could

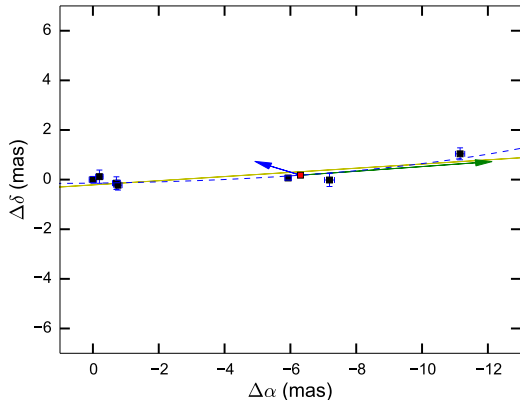


Fig. 5.— The observed VLA 1* positions, relative to the first detected epoch, with correction due to the trigonometric parallax. The position of VLA 1* at the reference epoch is plotted as a red square. The dotted curve shows the best fit after removing the movement of the trigonometric parallax. The proper motion and acceleration vectors are shown as green and blue arrows, respectively. The yellow line shows the expected movement of the star from the linear fit, without acceleration, after removing the trigonometric parallax.

contain a significant systematic error if VLA 1* happens to have a significant peculiar velocity relative to the rest of the Monoceros R2 cluster. In the same system, the velocity of Orion is $(u, v, w) = (-18.3, -15.6, -9.0) \text{ km s}^{-1}$. Thus, there does not appear to be an obvious relation between the relative velocities of the two regions. This does not discard a common origin, however, as dynamical evolution of expanding bubbles can be complex. As a final note, we would like to point out that while Monoceros is not normally associated with Gould’s Belt (e.g. Pöppell 1997), it does appear to be projected almost exactly along the plane defining Gould’s Belt (Figure 6). Its velocity vector is also almost entirely contained within the plane defining Gould’s Belt, and oriented mostly away from Gould’s Belt center, as would be expected if it participated in the overall expansion of that structure.

4.3. On the nature of VLA 1*

Our detection of a very compact non-thermal radio source close to peak position of the UCH II region VLA 1 (Gómez et al. 1998) is somewhat unexpected. Interestingly, this is not the first compact object seen in projection toward VLA 1. Gómez et al. (2000) used the VLA telescope to observe the GGD 12-15 region, and by removing the shortest baselines (i.e., removing the extended emission) they found a slightly resolved source near the center of the extended emission associated with VLA 1 (see Figure 7). This compact source, however, does not coincide in position with VLA 1*, as can also be seen in Figure 7. The separation between both sources is of $0''.55$ which is significantly larger than the position errors of the VLA images ($\sim 0''.1$; Gomez et al. 2000). The proper motion of VLA 1* over the 15 years separating the observations reported by Gómez et al. (2000) and our VLBA observations is expected to have been only $0''.08$, also insufficient to explain the separation between VLA 1* and the compact source reported by them. In addition, while the brightness temperature of the compact source detected by Gómez et al. (2000) is $\sim 200 \text{ K}$, that of VLA 1* is larger than 10^6 K . This further confirms that the two sources have a different nature.

Compact radio sources have been founded toward other UCH II regions: NGC 6334A (Carral et al. 2002; Rodríguez et al. 2014), NGC 6334E (Carral et al. 2002), and W3(OH) (Dzib et al. 2013, 2014). The source detected in W3(OH) is also thermal in nature, but those detected in NGC 6334A and NGC 6334E have been suggested to be non-thermal sources (Carral et al. 2002; Rodríguez et al. 2014). However, this is the first time that a compact source projected toward an UCH II region is imaged with the VLBI technique.

Massive stars are expected to be fully radiative. Thus, they are not expected to produce magnetically active coronas. On the other hand they can produce non-thermal radio emission in the strong shocks produced by the interaction of their jets with the surrounding medium (e.g., Carrasco-González et al. 2010) and in the wind-wind collision regions of two massive stars (e.g., Ortiz-León et al. 2011). The only well documented cases of jet-medium shocks show that they produce emission that is extended to sizes of around $1''$ level

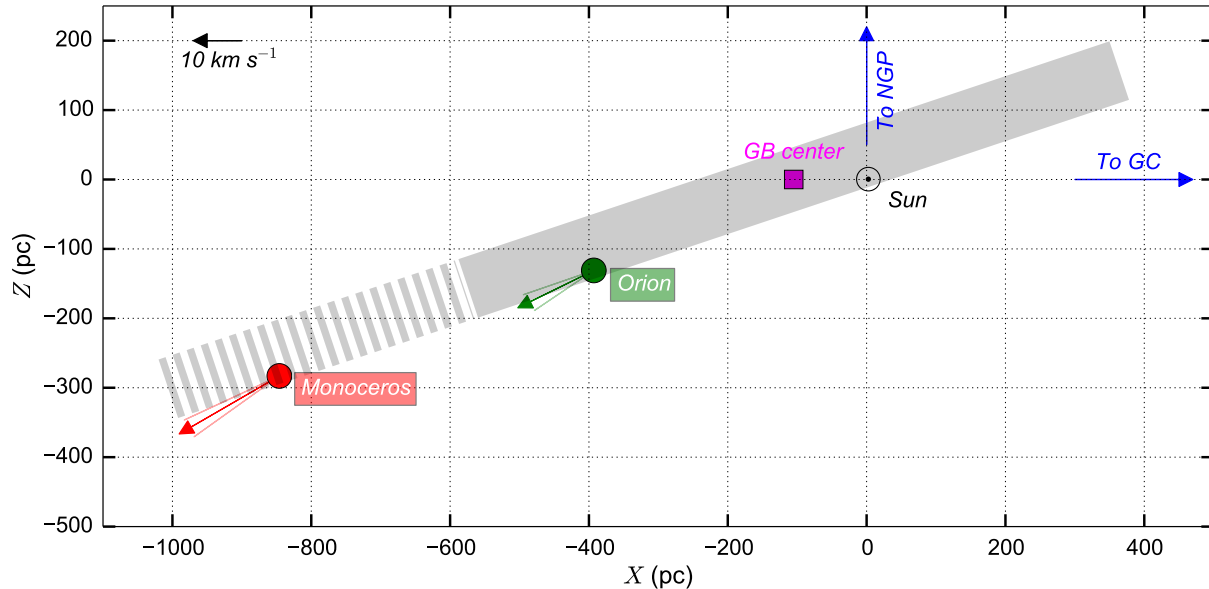


Fig. 6.— Position and velocity vectors of Monoceros and Orion in the Galactic (X,Z) plane with the reference frame centered on the Sun (see text for the definition of these axes). The grey band indicates the location of Gould’s Belt, with the center indicated by a magenta square. Stripes indicate the extension of the Gould’s Belt plane and shows that the position and velocity vectors of Monoceros lie in this plane. Blue arrows indicate the direction to the Galactic plane (GC) and to the northern Galactic pole (NGP).

(e.g., Carrasco-González et al. 2010; Wilner et al. 1999), that will be resolved out in VLBI observations. On the other hand, wind-wind collision regions have been imaged with VLBI and appear as resolved bow shock structures (Dougherty et al. 2005; Ortiz-León et al. 2011). At the distance of Monoceros such structures should be resolved if present, but this is not the case of the source reported here that shows, instead, a very compact structure in the seven detected epochs. The brightness temperature, size and variability of VLA 1* is similar to those detected for magnetically active intermediate- and low-mass YSOs (e.g., Loinard et al. 2008, Dzib et al. 2010). As a consequence, we suggest that this source is a magnetically active star (this explains, a posteriori, our choice of name, VLA 1*, for this source). With the data presented here, we cannot constrain the properties of VLA 1* further. In particular, it is unclear whether VLA 1* is physically associated with the UCH II region VLA 1, or if it is located behind or in front of it. Also, the mass of the star associated with VLA 1* remains entirely un-

constrained, as are the properties of the putative multiple system to which it belongs.

4.4. On the nature of the remaining compact radio sources

Most of the radio compact sources in GGD 12-15 were associated with magnetically active T Tauri stars by Gómez et al. (2002), due to their variability and spectral indices. The only exception was VLA 7 whose steady flux density and positive spectral index suggested a thermal radio emission produced by stellar winds. With the new radio observations, the non-thermal nature is confirmed for VLA 3, VLA 8, and VLA 10.

Adopting 5σ upper limits, the remaining five sources were not detected at levels of $90 \mu\text{Jy}$. This flux level is comparable to (or, in some cases, significantly lower than) the flux density reported by Gómez et al. (2002) for these sources. An explanation is that their flux levels during all the observations were lower than our threshold detection limit. This is feasible, since also the flux den-

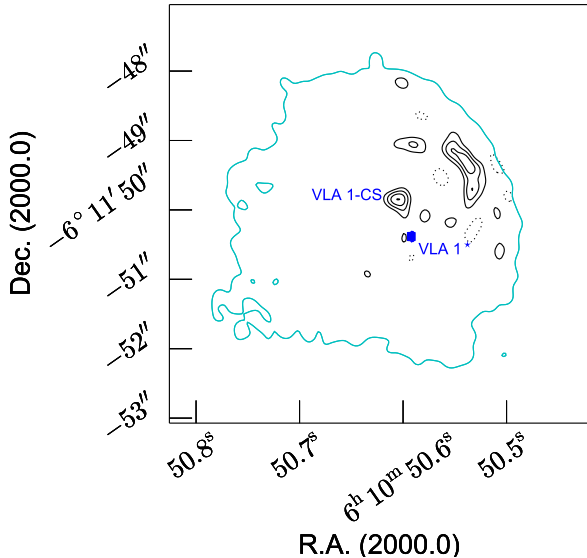


Fig. 7.— The VLA 1 cometary UCHII region as seen in the VLA continuum map at 8.4 GHz, as shown by Gómez et al. (2000). The cyan line is the border of the extended radio emission. The black contours trace the compact radio emission when visibilities shorter than 200k λ are removed. The compact source studied by Gómez et al. (2000) is labeled as VLA 1-CS. The blue square indicates the position of VLA 1*.

sity of VLA 3, VLA 8 and VLA 10 are below our threshold limit in almost all the epochs. Another explanation is that they are resolved out in our high resolution images. As a rough attempt to detect extended non-thermal radio emission from these sources, we produced images by only using the shortest baselines in the array (<80,000 k λ). No detection was obtained.

Finally, we should mention that our observations at 8.4 GHz are not ideal for these sources, given their negative spectral indices. New VLBI observations at longer wavelengths would help to clarify the nature of their radio emission. This would be possible using the new sensitive C-band (6 GHz) receivers installed on the VLBA antennas.

5. Conclusions

In this paper, we reported on VLBA observations of the cluster of compact radio sources associated with the UCHII region in GGD 12-15, also known as VLA 1, reported by Gómez et al. (2000, 2002). We detected a total of four sources. The sources VLA 3, VLA 8, and VLA 10 were detected only in single epochs, while a source projected inside VLA 1 was detected in seven different epochs. Given its radio properties, this source is likely to be a magnetically active star, that we call VLA 1*. Using the measured positions of VLA 1* in the seven detected epochs, we derive its proper motion and trigonometric parallax, ϖ . The best fit yields $\varpi = 1.12 \pm 0.05$ mas, that corresponds to a distance $d = 893^{+42}_{-40}$ pc. We argue that this is the most reliable distance measurement to the Monoceros R2 region to date.

G.N.O.-L, L.L., and L.F.R. acknowledge the financial support of DGAPA, UNAM, and CONACyT, México. L.L. and G.N.O.-L are indebted to the Alexander von Humboldt Stiftung for financial support. The National Radio Astronomy Observatory is operated by Associated Universities Inc. under cooperative agreement with the National Science Foundation.

REFERENCES

- Briggs, D. S. 1995, Bulletin of the American Astronomical Society, 27, 112.02. Available via <http://www.aoc.nrao.edu/dissertations/dbriggs/>
- Brunthaler, A., Reid, M. J., Menten, K. M., et al. 2011, *Astronomische Nachrichten*, 332, 461
- Carpenter, J. M., & Hodapp, K. W. 2008, *Handbook of Star Forming Regions, Volume I*, 4, 899
- Carral, P., Kurtz, S. E., Rodríguez, L. F., et al. 2002, *AJ*, 123, 2574
- Carrasco-González, C., Rodríguez, L. F., Anglada, G., et al. 2010, *Science*, 330, 1209
- Deller, A. T., Briske, W. F., Phillips, C. J., et al. 2011, *PASP*, 123, 275
- Dougherty, S. M., Beasley, A. J., Claussen, M. J., Zauderer, B. A., & Bolingbroke, N. J. 2005, *ApJ*, 623, 447

- Downes, D., Winnberg, A., Goss, W. M., & Johansson, L. E. B. 1975, *A&A*, 44, 243
- Dzib, S., Loinard, L., Mioduszewski, A. J., Boden, A. F., Rodríguez, L. F., & Torres, R. M. 2010, *ApJ*, 718, 610
- Dzib, S., Loinard, L., Rodríguez, L. F., Mioduszewski, A. J., & Torres, R. M. 2011, *ApJ*, 733, 71
- Dzib, S. A., Rodríguez-Garza, C. B., Rodríguez, L. F., et al. 2013, *ApJ*, 772, 151
- Dzib, S. A., Rodríguez, L. F., Medina, S.-N. X., et al. 2014, *A&A*, 567, L5
- Gómez, Y., Lebrón, M., Rodríguez, L. F., et al. 1998, *ApJ*, 503, 297
- Gómez, Y., Rodríguez, L. F., & Garay, G. 2000, *ApJ*, 531, 861
- Gómez, Y., Rodríguez, L. F., & Garay, G. 2002, *ApJ*, 571, 901
- Greisen, E. W. 2003, *Information Handling in Astronomy - Historical Vistas*, 285, 109
- Gyulbudaghian, A. L., Glushkov, Y. I., & Denisyuk, E. K. 1978, *ApJ*, 224, L137
- Herbst, W., & Racine, R. 1976, *AJ*, 81, 840
- Heiles, C. 1998, *ApJ*, 498, 689
- Loinard, L., Mioduszewski, A. J., Rodríguez, L. F., et al. 2005, *ApJ*, 619, L179
- Loinard, L., Torres, R. M., Mioduszewski, A. J., et al. 2007, *ApJ*, 671, 546
- Loinard, L., Torres, R. M., Mioduszewski, A. J., & Rodríguez, L. F. 2008, *ApJ*, 675, L29
- Loinard, L., Mioduszewski, A. J., Torres, R. M., et al. 2011, *Revista Mexicana de Astronomía y Astrofísica Conference Series*, 40, 205
- Menten, K. M., Reid, M. J., Forbrich, J., & Brunthaler, A. 2007, *A&A*, 474, 515
- Napier, P. J., Bagri, D. S., Clark, B. G., et al. 1994, *IEEE Proceedings*, 82, 658
- Ortiz-León, G. N., Loinard, L., Rodríguez, L. F., Mioduszewski, A. J., & Dzib, S. A. 2011, *ApJ*, 737, 30
- Prestage, R. M., Constantikes, K. T., Hunter, T. R., et al. 2009, *IEEE Proceedings*, 97, 1382
- Poppel, W. 1997, *Fund. Cosmic Phys.*, 18, 1
- Racine, R. 1968, *AJ*, 73, 233
- Racine, R., & van den Bergh, S. 1970, *The Spiral Structure of our Galaxy*, 38, 219
- Reid, M. J., & Brunthaler, A. 2004, *ApJ*, 616, 872
- Reid, M. J., Dame, T. M., Menten, K. M., & Brunthaler, A. 2016, *arXiv:1604.02433*
- Reid, M. J., & Honma, M. 2014, *ARA&A*, 52, 339
- Rozhkovskij, D. A., & Kurchakov, A. V. 1968, *Trudy Astrofizicheskogo Instituta Alma-Ata*, 11, 3
- Rodríguez, L. F., Moran, J. M., Ho, P. T. P., & Gottlieb, E. W. 1980, *ApJ*, 235, 845
- Rodríguez, L. F., Carral, P., Ho, P. T. P., & Moran, J. M. 1982, *ApJ*, 260, 635
- Rodríguez, L. F., Masqué, J. M., Dzib, S. A., Loinard, L., & Kurtz, S. E. 2014, *Rev. Mexicana Astron. Astrofis.*, 50, 3
- Torres, R. M., Loinard, L., Mioduszewski, A. J., & Rodríguez, L. F. 2007, *ApJ*, 671, 1813
- Torres, R. M., Loinard, L., Mioduszewski, A. J., & Rodríguez, L. F. 2009, *ApJ*, 698, 242
- Torres, R. M., Loinard, L., Mioduszewski, A. J., et al. 2012, *ApJ*, 747, 18
- Wilner, D. J., Reid, M. J., & Menten, K. M. 1999, *ApJ*, 513, 775